Astron. Astrophys. 363, 755–766 (2000)

ASTRONOMY AND ASTROPHYSICS

Low mass clouds in the Cepheus-Cassiopeia void

I. Khavtassi 15

Cs. Kiss[1,2], L.V. Tóth[1,2,3], A. Moór[1], F. Sato[4,5], S. Nikolić[6,7], and J.G.A. Wouterloot[8]

[1] Department of Astronomy of the Loránd Eötvös University, P.O. Box 32., 1518 Budapest, Hungary
[2] Max-Planck-Institut für Astronomie, Königstuhl 17, 69117 Heidelberg, Germany
[3] Helsinki University Observatory, P.O. Box 14, 00014 University of Helsinki, Finland
[4] Tokyo Gakugei University, Department of Astronomy and Earth Sciences, Koganei Tokyo 184-8501, Japan
[5] Institut d'Astrophysique Spatiale, bâtiment 121, Campus d'Orsay, 91405 Orsay Cedex, France
[6] Astronomical Observatory, Volgina 7, 11050 Belgrade, Serbia
[7] Onsala Space Observatory, 43992 Onsala, Sweden
[8] Radioastronomisches Institut der Universität Bonn, Auf dem Hügel 71, 53121 Bonn, Germany

Received 12 May 2000 / Accepted 7 September 2000

Abstract. We present the results of optical, far-infrared and radio observations of the small, non-star forming dark cloud Khavtassi 15, located in the Upper Cepheus–Cassiopeia region. We derive an average extinction of $\mathrm{A_V} = 1\overset{\mathrm{m}}{.}6$ and a distance of $250 \pm 25\,\mathrm{pc}$ from Digitized Sky Survey data and star counts using objective prism spectroscopy. A fully computerized algorithm was used for non-biased analysis of starcount data. A kinetic temperature of 7 K and a peak number density of $\mathrm{n(H_2)} = 5.9 \times 10^3\,\mathrm{cm^{-3}}$ were estimated from multiisotopic, multilevel CO measurements. CO measurements also revealed three main condensations inside the cloud. Kh 15 has a total gas mass of $34\,\mathrm{M_\odot}$ and it is most probably part of a shell seen as a FIR loop called GIRL126+10. We investigated the correlation among optical extinction, radio and FIR emission and masses derived for the dust and gas inside the cloud core. Stability analysis has shown, that Kh 15 is not far from gravitational virial equilibrium, and may be fully stabilized by the external pressure. In addition to Kh 15, the starcounts also indicate the presence of an extended nearby extinction layer at $\mathrm{d} \leq 150\,\mathrm{pc}$ which we consider as the wall of the Local Bubble (LB) towards the Upper Cepheus-Cassiopeia. Distances of the dark clouds LDN 1308, LDN 1333 and Khavtassi 19 are also estimated.

Key words: ISM: clouds – ISM: dust, extinction – ISM: molecules – ISM: individual objects: Kh 15 – ISM: individual objects: LDN 1308

1. Introduction

This paper is part of an extensive multiwavelength survey of low mass clouds (LDN 1235, LDN 1251, LDN 1274 (Nikolić et al. 2000, in prep.), Kh 20, etc.) in the Cep-Cas void (Grenier et al. 1989). Our main aims are to derive distances and investigate the differences in the morphology, chemical composition and physical properties of these clouds.

It is likely that molecular clouds interact with at least one shock front during their lifetime and form cores due to this trigger. Compression by stellar or supernova (SN) winds forms molecular clouds, triggers cloud collapse or may act indirectly speeding up the diffusion of the magnetic field (see e.g. Heathcote & Brand 1983). Several papers (see e.g. Kun & Prusti 1993; Sato et al. 1994; Tóth & Walmsley 1996) reported triggered star formation in the Upper Cepheus-Cassiopeia (UCC) region, the three main parts of which are: the Cepheus Flare giant molecular cloud (Hubble 1934; Lebrun 1986), the Cep-Cas void (a SN bubble; Grenier et al. 1989) and the Cassiopeia giant molecular cloud (Grenier et al. 1989). The latter CO survey was followed by the Nagoya ^{13}CO (1–0) survey (Yonekura et al. 1997), which revealed a large number of small clouds in the UCC region. Distances to the clouds inside the $15^\circ \times 15^\circ$ Cep–Cas void were not estimated so far. Tóth & Horváth (1996) investigated the morphology of 7 dark clouds towards the UCC region and found examples of slow shock-cloud interactions.

Kh 15 (Khavtassi 1955), located at $l = 122\overset{\circ}{.}7\; b = 9\overset{\circ}{.}6$ is one of these head-tail clouds found in the Cep-Cas void. It appears as an elongated opaque spot (with a size of $40' \times 20'$) on the POSS image (see Fig. 5) near another dark cloud, LDN 1308 (Lynds 1962). In the Atlas of Galactic Dark Clouds (Khavtassi 1960) no. 216 appears as an E-W elongated banjo-shaped feature which includes LDN 1308 and Kh 15. We investigated the most opaque western part, and the catalogue number, 15, is used accordingly.

The cloud is visible on the Dame et al. (1987) ^{12}CO integrated intensity map as a small bright spot. It was also detected in the ^{12}CO and ^{13}CO (J=1–0) survey of Taylor et al. (1987), where it is listed as TDS 473. In the Nagoya ^{13}CO (1–0) survey of the Cepheus–Cassiopeia region the cloud has been listed as no. 137 by Yonekura et al. (1997). Kh 15 has also been included

Send offprint requests to: Cs. Kiss (pkisscs@innin.elte.hu)

in the Catalogue of Infrared Excess Clouds (Désert et al. 1988) with the number 169.

We report the results of a multiwavelength study of Kh 15, including optical and infrared data and radio spectral line measurements in Sects. 2 and 3. We provide distance and optical extinction estimations derived by our new algorithm in Sect. 4, investigate the velocity distribution and calculate the molecular gas mass. In Sect. 5 we analyse the stability using the virial theorem. The distributions of the emission of dust and gas are also compared in this section.

2. Input data

2.1. Optical data

Schmidt Observations: We have obtained objective prism images of Kh 15 using the 60/90/180 cm Schmidt telescope of the Konkoly Observatory. The diameter of the field was 5° and it was centered at $\alpha(1950) = 0^{\rm h}49^{\rm m}30^{\rm s}$, $\delta(1950) = 73^\circ30'$. A UV transparent objective prism with a refracting angle of 5° and dispersion of 580 Å/mm at H_γ was used. The spectra were recorded on Kodak 103aO emulsion with 2mm widening. Two sets of images were taken with exposures of 16×2 minutes and 16×0.5 minutes. The observations were carried out in 1995, January 31. in the UT time interval 18:40–20:16 and in 1995, August 23. in the UT time interval 0:33–0:41, respectively. Visual magnitudes of all the classified stars (see Sect. 3) have been taken from the HST Guide Star Catalogue CD-ROM Version 1.1[1]. We identified the stars in the GSC using the SKYMAP software (version 2.7, by Doug Mink[2]).

Star count data: Coordinates, B and R magnitudes of stars within $1^\circ \times 1^\circ$ and $\sim$3.5 deg^2 fields (both centered at $\alpha(1950) = 0^{\rm h}45^{\rm m}27^{\rm s}$, $\delta(1950) = +72^\circ11'56''$, the reference position of the radio measurements) were obtained from the electronic version of the USNO A2.0 catalogue [3].

2.2. IRAS data

The distribution of the FIR radiation at 12, 25, 60 and 100 μm wavelength was studied using ISSA images (Wheelock et al. 1994) with angular resolution of $1'$ to $4'$ and a uniform pixel size of $1\farcm5$. Far-infrared (FIR) point sources within the Kh 15 area were searched in the IRAS Point Source Catalogue[4]. We also analysed 12, 25, 60 and 100 μm high resolution (HIRES) IRAS images provided by the Infrared Processing and Analysis Center (IPAC).

COBE-DIRBE annual average maps (AAM) at 60 and 100 μm were used in order to calibrate ISSA and HIRES maps. AAM maps have been obtained from the NASA Gothard Space Flight Center ftp site[5].

2.3. CO data

Nagoya-4m observations: We observed Kh 15 in the ^{13}CO (J=1–0) line, using the 4m millimeter-wave telescope at Nagoya University in 1991 January and December as part of mapping observations of the Cepheus molecular cloud complex. The half-power beamwidth of the telescope was $2\farcm7$ with a main beam efficiency of 0.7 at 110 GHz. The front-end of the receiver consisted of a 4 K cooled SIS mixer operated in the single-sideband (SSB) mode with the image sideband suppressed by more than 10 dB (Ogawa et al. 1990). The system noise temperature was $\sim$ 150 K (SSB) toward the zenith. An ambient-temperature chopper wheel was used to determine the antenna temperature scale. To estimate the excitation temperature of the CO gas, we observed in April 1992 the centre of the ^{13}CO cloud in the ^{12}CO (J=1–0) line with the same equipment. The observations were made by using frequency switching over 13 MHz (corresponding to $\sim$ 35kms^{-1} at 110 GHz). We used an acousto-optical spectrometer (AOS) as a backend. The bandwidth of the AOS is 40 MHz, divided into 1024 channels. The effective frequency resolution was 40 kHz, equivalent to a velocity resolution of 0.11 $\rm kms^{-1}$ at 110 GHz. In reducing the spectral data, we subtracted baselines of third-order polynomials.

An area of $\sim$ 0.13 deg^2 was mapped in the ^{13}CO line covering the main part of Kh 15 cloud with a grid spacing of $2'$ in galactic coordinates. The number of observed points was 124. The integration time per point was typically 20–30 s in 1991 January, while it was $\sim$80 s in 1991 December due to the poor weather conditions. The resulting r.m.s. noise level was typically 0.2 K. For ^{12}CO (J=1–0) an r.m.s. noise level of 0.29 K was obtained after an integration of 7 min. Sample spectra are given in Fig. 2 (see also Sect. 3.3).

In order to monitor the system performance and calibrate the antenna temperature, we observed the source S 140 at about hourly intervals. Its adopted radiation temperatures, $T_{\rm R}^*$, were 20 K and 9 K for the ^{12}CO and ^{13}CO (J=1–0) lines, respectively. They include the coupling of the antenna beam pattern with the brightness distribution in the source.

Onsala-20m observations: We observed the ^{13}CO (J=1–0) and the C^{18}O (J=1–0) lines using the Onsala Space Observatory (OSO) 20-m telescope in March, 1998. The receiver was an SIS mixer with a typical $T_{\rm rec}$=100 K (SSB) in the used frequency range. We used a 1600-channel autocorrelator with 40MHz bandwidth corresponding to a velocity resolution of 0.068 $\rm kms^{-1}$. At 110 GHz the telescope has a HPBW of $35''$, with a beam efficiency of 0.8. The pointing was checked by observing the SiO maser source T Cep and we estimated the pointing uncertainty to be about $3''$ r.m.s. in Az. and El. The ob-

[1] The Guide Star Catalog (GSC) was prepared by the Space Telescope Science Institute (STScI), 3700 San Martin Drive, Baltimore, MD 21218, USA. STScI is operated by the Association of Universities for Research in Astronomy, Inc. (AURA), under contract with the National Aeronautics and Space Administration (NASA).

[2] Harvard-Smithsonian Center for Astrophysics

[3] available at the URL:"http://www.nofs.navy.mil"

[4] Astronomical Data Center CD-ROM, Selected Astronomical Catalogs, Vol. 1

[5] available at the ftp-address: "ftp.gsfc.nasa.gov"

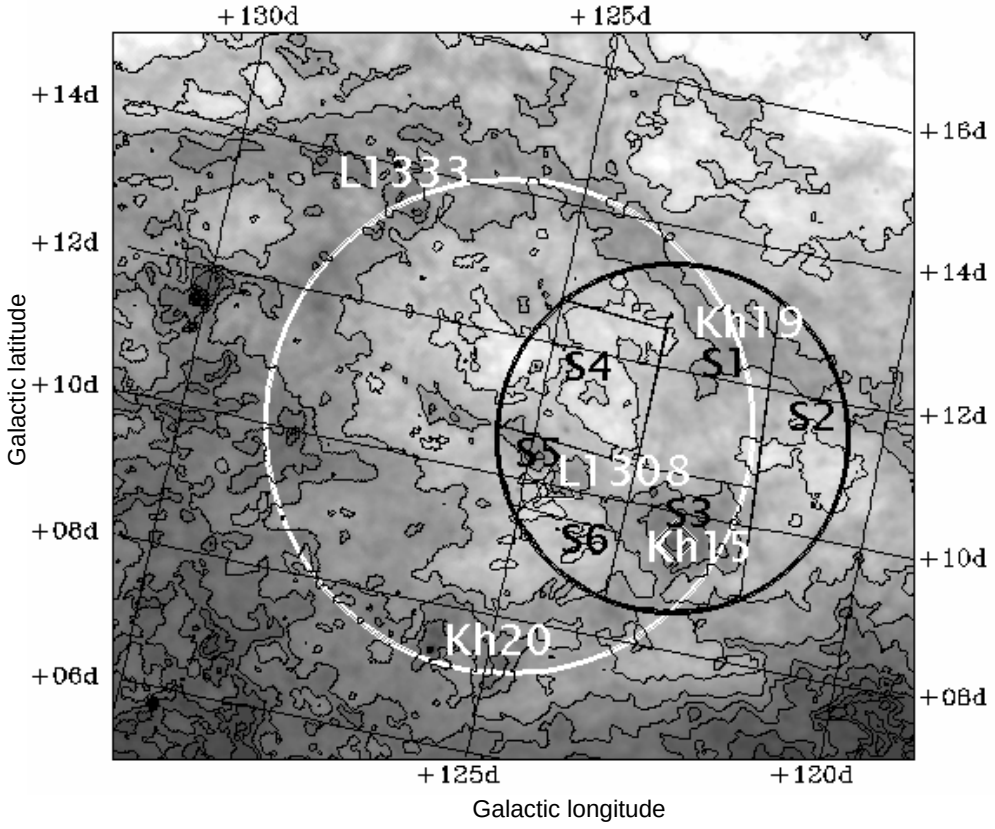

Fig. 1. IRAS 100 μm image of the region around Kh 15 (ISSA data). The 5° diameter field of the Schmidt plate is marked with a black circle. An IRAS loop GIRL126+10 (Tóth et al. 1996) is marked with an ellipse drawn with a thick white line. Contours are drawn from 6 MJysr^{-1} with steps of 3 MJysr^{-1}. We have indicated Kh 15 in association with the $\sim 7^\circ$ diameter loop GIRL126+10 and with a string of cloudlets running through the dark cloud LDN 1308 (Lynds 1962). S1–S6 mark the six subfields of the Schmidt-plate (see Table 1).

servations were made in a frequency switching observing mode, with -6 MHz frequency throw. The chopper-wheel method was used for the calibration, and the intensity scale is given in terms of T_R^*. We mapped the central region of Kh 15 (see Fig. 6) with a variable 1′ and 0.′5 spacing in the ^{13}CO (J=1–0) (129 positions) and the C^{18}O (J=1–0) (99 positions) transitions. The r.m.s. noise was typically 0.4 K for ^{13}CO and 0.15 K for C^{18}O. We subtracted linear baselines.

KOSMA-3m observations: ^{12}CO (J=2–1) and (J=3–2) spectra were measured with the old University of Cologne 3m telescope. ^{12}CO (J=2–1) data were obtained at two positions in December, 1995. The half-power beam width of the antenna at the CO (2–1) and CO (3–2) transitions was 125″ and 70″ respectively. The telescope and the instrumentation are described in detail in Winnewisser et al. (1990). Spectra obtained at the position of Nagoya's ^{12}CO (1–0) measurement are shown in Fig. 2. The velocity resolution was 0.22 kms^{-1} and 0.14 kms^{-1} for the ^{12}CO (2–1) and ^{12}CO (3–2) transitions, respectively. A small (5 pos. × 5 pos.) map was made in the ^{12}CO (J=3–2) line in March, 1998, using the new KOSMA telescope (after refurbishing), centered at the same sky position as in 1995 (the telescope and the instrumentation are described in detail in Kramer et al. 1998). Using the new KOSMA telescope we have made a measurement of LDN 1308 in the ^{12}CO (2–1) transition in September 1999. The measurement were made at three positions ((l, b) = (124.°9, 10.°4), (124.°4, 10.°2), (124.°59, 10.°13)) in position switching mode, using the 230/345 GHz dual channel SIS receiver, with a velocity resolution of 0.21 kms^{-1}. The r.m.s. noise was about 0.2 K at the T_{mb} scale.

3. Data analysis

3.1. Optical data

3.1.1. Wolf diagrams

We have divided the field of the Schmidt plate into 6 subfields (see Fig. 1 and Table 1) in order to study the spatial variations of the extinction.

Classification of stellar spectra on the objective prism images was made by eye using the set of criteria of the Bonner Spectral Atlas II. (Seitter 1975). We have classified 768 B to K type stars. We estimate the accuracy of the spectral classification for B, A and F stars (13, 240 and 137 stars, respectively) to be ~ 2 spectral subclasses, which means $\sim \pm 0.^m4$ in M_V and ρ for A type stars. Our sample is complete down to $V = 12.^m0$ for A type stars. We have assigned absolute magnitudes M_V to all the classified stars (Lang 1992) and derived apparent distance moduli $\rho = V - M_V$.

Using these results we drew Wolf diagrams (Wolf 1923) in order to estimate the apparent distance moduli at which the presence the of the extinction layers cause a distortion on the curve of the $\log N(V)$ function i.e. the logarithm of the cumulative star counts as a function of the distance modulus ρ (see Fig. 4). The cutoff in the $\log N(V)$ curve for $\rho > 9^m$ is due to the limiting magnitude of our observations. On the other side, due to the small number of classified stars for low distance moduli, the

Table 1. Schmidt plate subfields. Columns are: (1) number of the subfield; (2)-(3) galactic coordinates; (4) average surface brightness at 100 μm from the ISSA image; (5) area of the subfield; (6) number of B, A and F -type stars inside the subfield; (7) comments, e.g. associated objects. See also Fig. 1

subfield	l $^\circ$	b $^\circ$	I_{100} MJysr^{-1}	area deg^2	Number of B,A,F stars	comment
1	122.9	12.1	13.8	5.7	115	NW-part of GIRL126+10 and Khavtassi 19
2	121.2	11.1	13.1	3.8	82	low FIR emission region (reference)
3	122.6	9.6	16.8	3.5	77	Khavtassi 15
4	124.4	11.6	11.3	3.9	62	low FIR emission region (reference)
5	124.5	10.1	14.3	1.9	30	LDN 1308 dark cloud and a string-like cloudlet
6	124.1	9.2	12.3	1.0	21	low FIR emission region (reference)

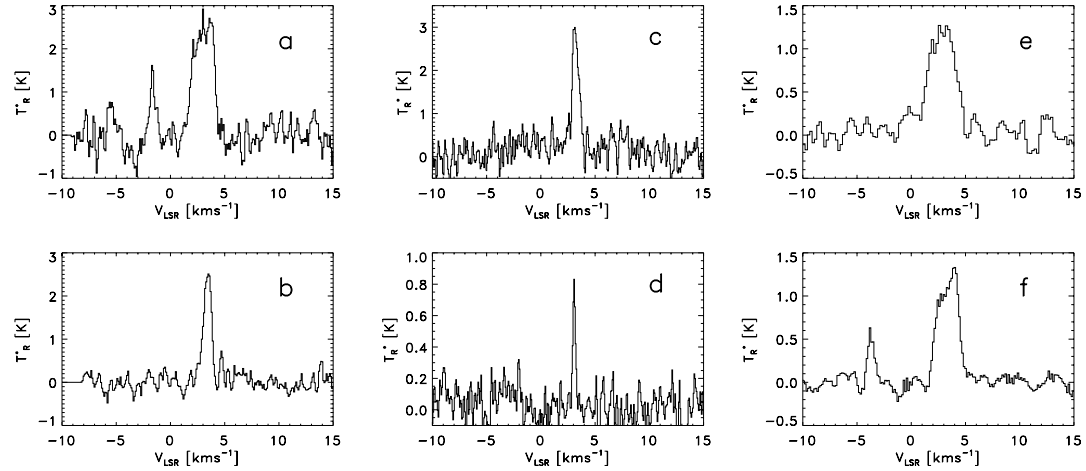

Fig. 2a–f. Sample spectra of Kh 15 at (l, b) = (122.°73, 9.°60)
a and **b**: Nagoya-4m telescope (HPBW = 2.′7), ^{12}CO (1–0) and ^{13}CO (1–0)
c and **d**: Onsala-20m telescope (HPBW = 0.′5), ^{13}CO (1–0) and C^{18}O(1–0)
e and **f**: KOSMA-3m telescope, ^{12}CO (2–1) and ^{12}CO (3–2) spectrum at (l, b) = (122.°73, 9.°63), HPBW = 2.′2 and 1.′1, respectively.

proper distance of the extinction features closer than $\rho = 6^{\rm m}$ cannot be identified. The corresponding distance of 150 pc is therefore an upper limit of their distance.

The extinction free curve was created using an extended galaxy model by Wainscoat (1992) (also Balázs 1998, priv. com.). In this way one can estimate the cumulative star counts for any spectral type within a region anywhere in the sky. The effect of an extinction layer is simply a shift towards higher distance moduli, and the measure of this shift is the average extinction caused by the layer itself. Best fit values for the distance and extinction of each subfield are presented in Table 4.

3.1.2. Visual extinction from POSS data

A blue extinction map was created by counting stars on a POSS blue plate (see Sect. 2.1) in the $1^\circ \times 1^\circ$ area around Kh 15. The visual extinction A_V was calculated using the method described by Dickman (1978b). The spatial resolution was $3' \times 3'$ corresponding to the size of the reseau. We derived a value for reference star counts from the "non-cloudy" parts of the POSS plate. Another larger field around Kh 15 was analysed at a lower spatial resolution of $15' \times 15'$ in order to derive an average value of A_V and compare it with the visual extinction obtained from the Wolf diagrams.

3.2. FIR data

Before using the ISSA and HIRES data all the maps have been calibrated using the COBE maps at appropriate (60 and 100μm) wavelengths. In the first step ISSA images were calibrated with the help of COBE-DIRBE annual average maps (AAM) (Hauser et al. 1998), following the information available at the COBE homepage[6]. Determination of the zodiacal background emission on the DIRBE images was done by using the IRSKY[7] software (Ebert 1994). We assumed linear relationships. As a second step, calibrated ISSA maps were used to calibrate the HIRES maps to the COBE scale. Table 2 summarizes the resulting coefficients and levels of correlation.

Using the HIRES and ISSA 60 and 100 μm images, we made 100 μm excess, $\Delta I_{100} = I_{100} - I_{60}/\Theta$, maps (Laureijs et al. 1989). We derived the value of Θ at the outer parts of Kh 15 and obtained $\Theta = 0.21 \pm 0.02$.

[6] http://space.gsfc.nasa.gov/astro/cobe/cobe_home.html
[7] provided by IPAC

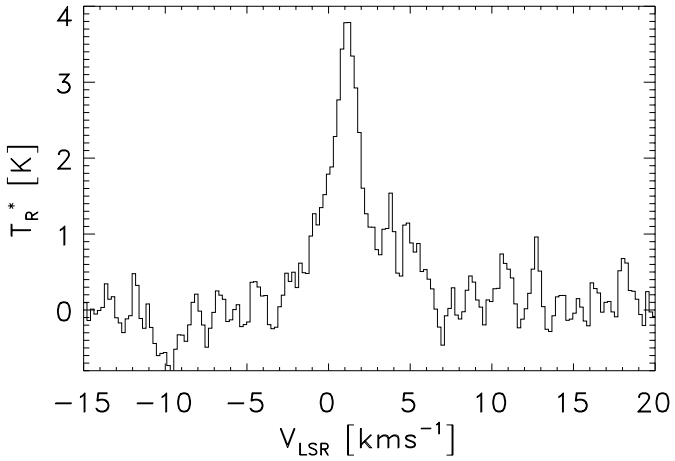

Fig. 3. KOSMA-3m (HPBW=2′.2) spectrum of LDN 1308 towards l=124°.9, b=10°.4, of the ^{12}CO $(2-1)$ line. HPBW=2′.2.

Table 2. Results of COBE-ISSA-HIRES calibrations. We assumed linear relationships in all cases. The conversion is DIRBE = slope×ISSA + const. and ISSA = slope×HIRES + const.

from ISSA to	slope	const. MJysr^{-1}	corr.
DIRBE 60 μm	0.88 ± 0.05	-0.7 ± 0.1	0.95
DIRBE 100 μm	0.72 ± 0.03	-1.5 ± 0.1	0.96
from HIRES to	slope	const. MJysr^{-1}	corr.
ISSA 60 μm	0.70 ± 0.06	2.0 ± 0.2	0.91
ISSA 100 μm	0.73 ± 0.07	12.6 ± 0.4	0.91

3.3. CO data

Fig. 2 shows the profiles of the ^{12}CO and ^{13}CO (J=1–0) lines taken at (l, b) = (122°.73, 9°.60), the position where the ^{13}CO integrated intensity has a maximum on the Nagoya map (see Fig. 6). In the Nagoya ^{12}CO spectrum, one can see two emission peaks at $v_{LSR} \approx 3$ and -1.8 kms^{-1}. The former, more intense and much broader peak, has a prominent ^{13}CO counterpart, and it seems likely that it is emitted by the molecular gas in the Kh 15 cloud. The weaker velocity component is telluric line, also seen in the ^{12}CO (3–2) line observed with the KOSMA telescope. Table 3 lists the parameters of the three CO isotopic lines at $v_{LSR} \approx 3$ kms^{-1} obtained by fitting single Gaussians. A spectrum showing the strongest line of the KOSMA-3m observation of LDN 1308 is presented in Fig. 3.

4. Results

4.1. Extinction and distance

4.1.1. Distances from Wolf diagrams

The Wolf diagrams (Fig. 4) suggest the presence of several extinction layers, which are listed in Table 4. Extinction and distance values were derived by placing a weak extinction feature ($0^m.01$) into the model Wolf diagram at a given distance modulus. This step was repeated until the difference between model and observed curves became small enough, in our case until $|N_{obs}(\rho) - N_{mod}(\rho)| \leq \epsilon$, $\epsilon = 1$. Our distances differ slightly from the ones using Wolf's original distance interpretation, since our method derives the distribution of the extinction along the line of sight, and not only determines the distance

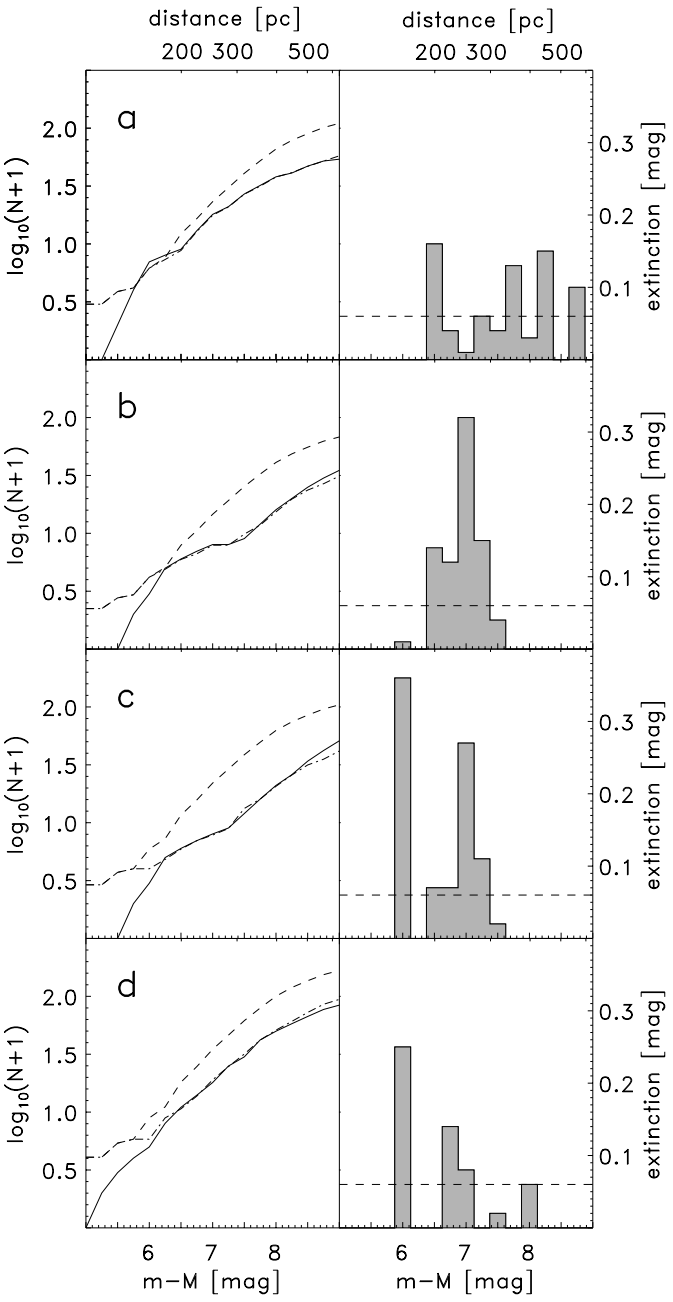

Fig. 4a–d. Wolf diagram (left) and distribution of visual extinction along the line of sight (right). In the Wolf diagrams the continuous curves present the observed star counts. Dashed and dotted curves present the extinction-free and -modeled star count curves (see Table 4 and Sect. 4.1). The dashed horizontal line in the extinction distribution figures represent the experimental detection limit ($\sim 3\sigma$).
a for Subfield 1; **b** for Subfield 3 (Kh 15); **c** for Subfield 3 and 5 (Kh 15 and LDN 1308); **d** for the reference fields 2, 4 and 6;

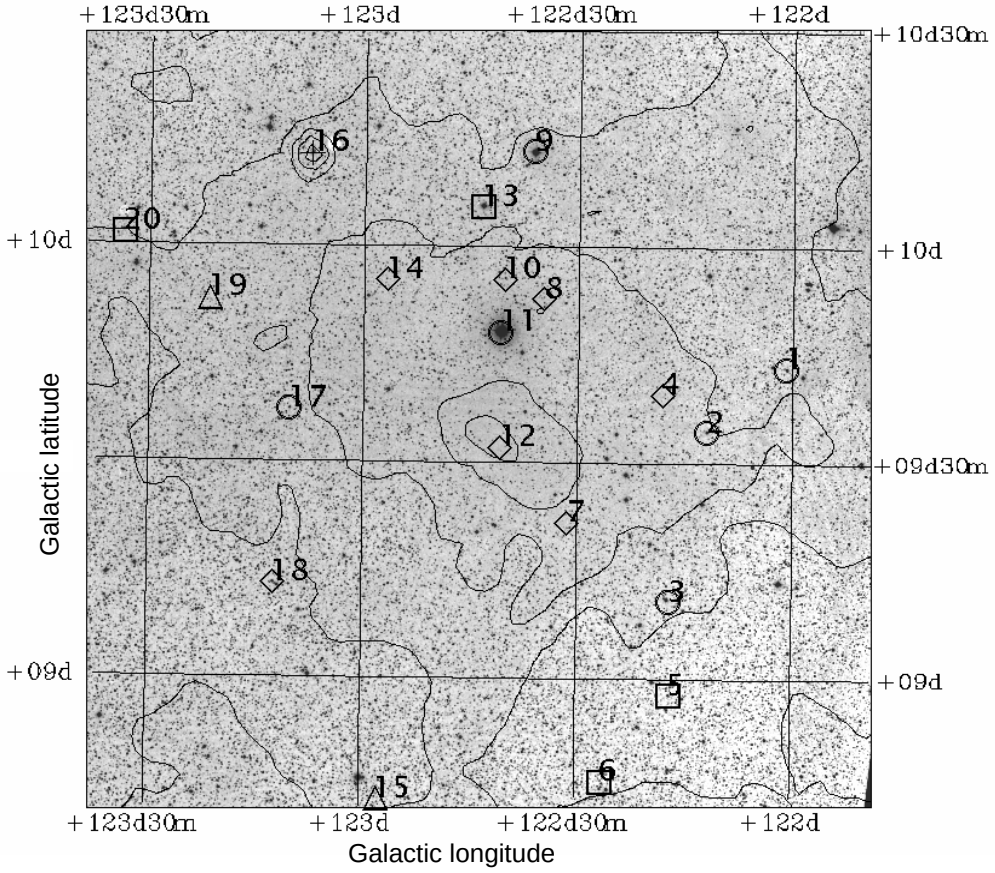

Fig. 5. Location of IRAS point sources near Kh 15 on the POSS (Palomar Observatory Sky Survey) image. Contours show the 100 μm emission from 11.3 MJysr^{-1}, with 4 MJysr^{-1} steps (ISSA image without galactic background subtraction). Point sources marked by circles have star-like IRAS colours; point sources marked by diamonds, boxes and triangles have good flux quality (3) only at 100, 60 and 25μm, respectively. Point source no. 16 (signed by a cross) is identified as the galaxy MCG+12-02-001 (see the text for details).

Table 3. Overview of the CO measurements and characteristic line parameters.

line	T_R^* (K)	v_{LSR} (kms^{-1})	Δv (kms^{-1})	l (°)	b (°)	$v_{resolution}$ (kms^{-1})	beam arcmin	Telescope
^{12}CO (J=1–0)	3.9	3.0	2.3	122.73	9.60	0.11	2.7	Nagoya-4m
^{13}CO (J=1–0)	3.0	3.4	0.8	122.73	9.60	0.11	2.7	Nagoya-4m
^{13}CO (J=1–0)	2.9	3.1	0.8	122.73	9.60	0.068	0.5	Onsala-20m
C^{18}O (J=1–0)	0.7	3.0	0.3	122.73	9.60	0.068	0.5	Onsala-20m
^{12}CO (J=2–1)	1.2	2.5	2.6	122.73	9.63	0.22	2.2	KOSMA-3m
^{12}CO (J=3–2)	1.7	3.2	2.0	122.73	9.63	0.14	1.1	KOSMA-3m

moduli where breaking points appear on the cumulative star-count curve.

Distance of Kh 15: We assign the strongest feature in the Wolf-diagram of Subfield 3 (Table 4 and Fig. 4b) to Kh 15 appearing at $\rho = 7\overset{\mathrm{m}}{.}0$ (250 pc). According to the FIR map Fig. 1, the other weaker features around Kh 15 probably contain the extinction caused by the wall of GIRL126+10.

Distance of the loop GIRL126+10: On the Wolf diagram containing the northwestern part of GIRL126+10, (Subfield 1, Fig. 4a) one can see several extinction features, the strongest one being at the distance modulus $\rho = 6\overset{\mathrm{m}}{.}5$ (200 pc). This feature can also be seen on the Wolf-diagram of Subfield 3 (see above), which also contains a part from GIRL126+10. Furthermore, there are other distance measurements of different parts of GIRL126+10. Obayashi et al. (1998) reported a distance of 180 pc for LDN 1333, which is located at the eastern part of GIRL126+10 (see Fig. 1). The extinction seen on their Fig. 1 is quite extended in space, and therefore the derived 180 pc distance is in a good agreement with our distance derived for this layer. Therefore we adopt 200 pc as GIRL126+10's distance, which gives a diameter of about 25 pc for the 7° sized loop.

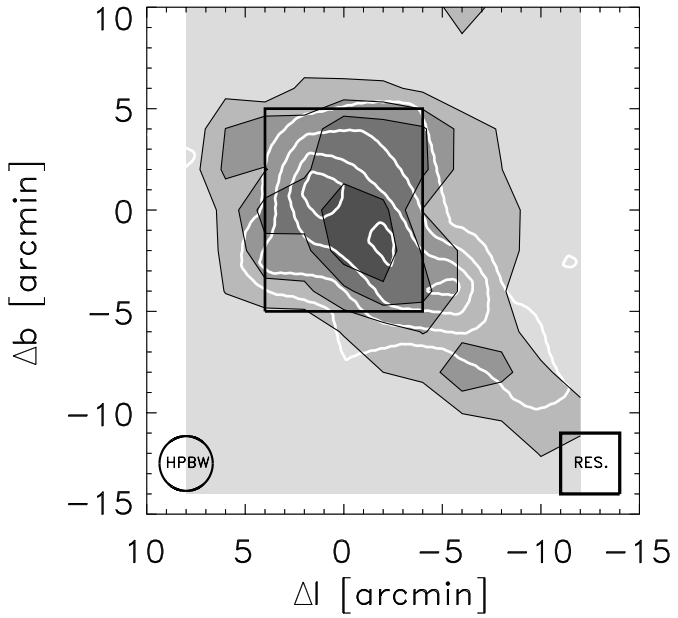

Fig. 6. *Grayscale with black contours:* ^{13}CO (1–0) integrated intensity map of Kh 15 (Nagoya-4m), centered at (l, b) = (122.°73, 9.°60), the velocity interval is: $1\,\mathrm{kms}^{-1} \leq \mathrm{v_{LSR}} \leq 5\,\mathrm{kms}^{-1}$. Contours are from $0.5\,\mathrm{Kkms}^{-1}$ with $0.5\,\mathrm{Kkms}^{-1}$ steps and the beam size is indicated in the bottom-left corner. The $8' \times 10'$ sized rectangle indicates the area mapped with OSO-20m (see Fig. 7).
White contours: blue extinction map of Kh 15. Contours are from $1\overset{\mathrm{m}}{.}6$ with $0\overset{\mathrm{m}}{.}4$ steps. The center of the field is the same as above. The square in the bottom-right corner indicates the size of the reseau.

Distance of LDN 1308: Since the subfield containing LDN 1308 (Subfield 5) is rather small, we were not able to construct a Wolf diagram only from the stars counted within this region. In order to increase the number of stars, we added the data of Subfields 3 and 5, and drew a common Wolf diagram (see Fig. 4c and Table 4). It shows a nearer and a more distant layer ($\rho \leq 6\overset{\mathrm{m}}{.}0$ ($\leq 150\,\mathrm{pc}$) and $\rho = 7\overset{\mathrm{m}}{.}0$ ($250\,\mathrm{pc}$)). Since at $\rho \leq 6\overset{\mathrm{m}}{.}0$ no extinction can be seen in the Wolf diagram of Subfield 3, we identify the closer layer as the extinction of LDN 1308. The further layer is the effect of Kh 15. The distance of LDN 1308 cannot be determined more accurately due to the small star numbers at low distance moduli. Because of the size of GIRL126+10 and the upper limit of the distance of LDN 1308 it does not appear that LDN 1308 is physically connected with GIRL126+10 or Kh 15.

4.1.2. The extinction distribution

The visual extinction resulting from star counts of a POSS image (see Sects. 2.1 and 3.1.2) is shown in Fig. 6 as white overlaying contours. The resulting maximum value of $\mathrm{A_V}$ is $2\overset{\mathrm{m}}{.}4$, derived as $\mathrm{A_V^{max}} = 0.76 \times \mathrm{A_B^{max}}$(Dickman 1978b). We shall compare $\mathrm{A_B}$ with $\mathrm{I_{100}}$ in Sect. 5.1. For the average value of $\mathrm{A_V}$ around Kh 15 in the larger, approximately 3.5 deg^2 sized POSS field, we obtained a value of $\mathrm{A_V^{ave}} = 0\overset{\mathrm{m}}{.}74 \pm 0\overset{\mathrm{m}}{.}1$, which is in a good agreement with the value of $0\overset{\mathrm{m}}{.}78$, derived as the sum of the extinction values seen at the Wolf diagram of Subfield 3, which contains Kh 15.

Table 4. Properties of the main extinction layers derived from the Wolf diagrams for six subfields (See Fig. 1). The columns are: (1) Name of the subfield(s); (2) distance modulus of the extinction layer (non-biased fit); (3) corresponding distance; (4) value of visual extinction derived from the Wolf diagram. The error of this extinction value is estimated to be $0\overset{\mathrm{m}}{.}05$ for all the layers.

Subfield	$(\mathrm{m}-\mathrm{M})$ (mag)	distance (pc)	$\mathrm{A_v^{Wolf}}$ (mag)
1	6.5	200±20	0.16
	7.8	360±40	0.13
	8.3	450±50	0.15
	8.8	560±60	0.10
3	6.5	200±20	0.14
	7.0	250±25	0.32
3+5	≤6.0	≤150	0.36
	7.0	250±25	0.28
2+4+6	≤6.0	≤150	0.25
	6.8	220±20	0.15

4.2. Far-infrared results

IRAS point sources: Towards Kh 15 we found twenty point sources, which are shown in Fig. 5. The point sources nrs. 1, 2, 3, 9, 11 and 17 (marked by open circles) have good or moderate flux quality in at least two bands, and may be classified as stars according to Walker et al. (1989). Each of them coincides with a star on the POSS image. Point source no. 16 (IRAS 00506+7248) has good (3) flux quality in all bands, and it has been identified as the galaxy MCG+12-01-001. Other sources have poor flux qualities at three of the four wavelengths. Point source no. 12 (IRAS 00449+7208) is located at the very centre of the Kh 15 cloud core and has been detected only at 100 μm by IRAS. Additional FIR observations would be needed to detect the source in other bands, and determine its nature. We assume it to be a small sized cold core and not an embedded (proto)star in Kh 15.

Large-scale structure: We have studied the large-scale structure of the interstellar dust towards Kh 15 using the IRAS maps. We present the ISSA 100 μm image of the region around Kh 15 in Fig. 1. The r.m.s. noise in this 100 μm image is 0.62 MJysr^{-1}.

Fig. 1 shows that Kh 15 may be associated with the $\sim 7^\circ$ diameter loop GIRL126+10 (Tóth et al. 1996), and with a string running NE-SW through LDN 1308 and Kh 15.

We analysed the 12, 25, 60 and 100μm high resolution IRAS images (HIRES), and found that the cloud was not detected at 12 and 25 μm (the mean value of the excess intensity is about the same as the standard deviation). At 100 μm Kh 15 is well-resolved and shows a clumpy structure. The 100 μm resolution was about $\sim 75''$.

Dust properties: We constructed an I_{cold} map (I_{cold} = $1.67\times(I_{100} - I_{60}/0.21)$, see Boulanger et al. 1998), using the 60 and 100 μm COBE calibrated HIRES images, presented in Fig. 7 as white overlaying contours. The scaling factor corrects for the fraction of the 100 μm emission which is lost in the subtraction. Therefore we used I_{cold} in the following instead of the 100 μm excess ΔI_{100} to calculate the parameters of the dust, especially the dust mass. I_{cold} is free of the radiation coming from smaller sized grains (the so called cirrus component), therefore one can assume that its total emission can be described by one grain family, the big grains (see e.g. Désert et al. 1990), and only by one dust temperature. Since much of the 60 μm emission originates from smaller grain emission at higher temperatures, it cannot be used to derive the dust temperature.

Lagache et al. (1998) found, that the FIR emission of the interstellar cold dust can be described by two components. One of these is associated with the galactic cirrus, shows good correlation at the 60 and 100 μm IRAS bands and its radiation can be described by a 17.5±1.5 K temperature, assuming a grey body spectral energy distribution (SED), with ν^2 emissivity law. The other component is in particular present in the direction of molecular regions and its dust temperature is around 15 K, assuming the same SED as before. Using I_{cold}, we separated this component from the FIR emission. Since we cannot determine the dust temperature of this component for Kh 15, we applied a uniform value of 15 K (the mean value according to Lagache et al., 1998), where $I_{cold} \geq 5\,\mathrm{MJysr^{-1}}$ ($\sim 3\,\sigma$ level over the background). Using these, we could estimate the 100 μm optical depth, the dust column density and mass (Hildebrand 1983). Because our cloud is small and has a relatively low density, we also calculated the 100 μm optical depth assuming an upper limit for the dust temperature of 17 K (see Fig. 7. in Lagache et al. 1998). The resulted cold dust masses are m_{cold} = 0.35 $M_\odot$ and m_{cold} = 0.12 $M_\odot$ using a uniform dust temperature of 15 K and 17 K, respectively, over the Kh 15 core region. The I_{cold} contours in Fig. 7 show three small cores with strong emission (denoted on the figure by C1, C2 and C3). The estimated masses of the C1, C2 and C3 cores are ~ 8, ~ 9 and ~ 7 percents of the total dust mass of this area, respectively.

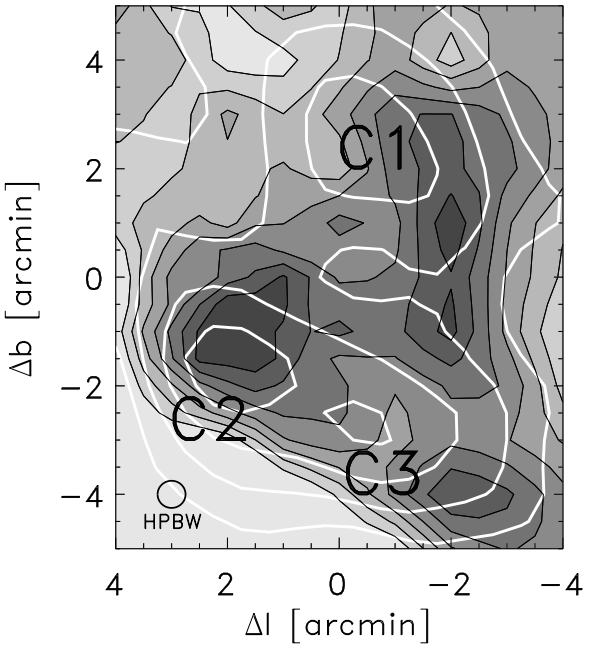

Fig. 7. *Grayscale with black contours:* $^{13}\mathrm{CO}\,(1-0)$ integrated intensity map (OSO-20m). Contours are from 1.5 $\mathrm{Kkms^{-1}}$ with 0.25 $\mathrm{Kkms^{-1}}$ steps, the velocity interval is 1 $\mathrm{kms^{-1}} \leq v_{LSR} \leq$ 5 $\mathrm{kms^{-1}}$. The center of the map is l=122.°733, b=9.°601. The beam size is indicated in the bottom-left corner.
White contours: I_{cold} map of the central part of Kh 15, made from the 60 and 100 μm HIRES images. Contours are from 7.0 $\mathrm{MJysr^{-1}}$ with 2.0 $\mathrm{MJysr^{-1}}$ steps. The center of the map is the same as above. The spatial resolution was estimated to be 75″. The 5.0 $\mathrm{MJysr^{-1}}$ contour, over which the mass estimation was done, approximately encircles the region presented here.

4.3. Molecular cloud

Nagoya-4m: Fig. 6 shows the Nagoya-4m integrated intensity map of the ^{13}CO (1–0) emission. The ^{13}CO cloud has a size of 20′×15′, and is elongated in the NE-SW direction. The velocities at the ^{13}CO line peaks vary systematically in the SW–NE dierction from 2.8 to 3.2 $\mathrm{kms^{-1}}$ in Kh 15. The central velocity of the line at the cloud centre is $v_{LSR} \approx 3.2\,\mathrm{kms^{-1}}$. We define the boundary of the molecular cloud at the $0.5\,\mathrm{Kkms^{-1}}$ level in Fig. 6, i.e. approximately at the 6σ level. The physical parameters of the ^{13}CO cloud core are summarized in Table 5. Assuming local thermodynamic equilibrium, we estimated kinetic temperatures and ^{13}CO column densities following Nozawa et al. (1991). We assumed a uniform excitation temperature (T_{ex}) throughout the core using the value derived at the cloud centre. It is difficult to choose the appropriate ratio of the H_2 column density $N(H_2)$ and the ^{13}CO column density N(^{13}CO). Since Kh 15 is relatively small and isolated, it is expected, that the relative abundance of the CO isotopes is lower than in larger and more complex star forming regions (see e.g. Tóth et al. 1995 and Harjunpää & Mattila 1996). Therefore we used $N(H_2)\,/\,N(^{13}CO) = 1.2\times10^6$ to calculate the molecular hydrogen column densities, which is a median value from the papers sited above. It should be noticed that the densities and masses estimated below are highly dependent on the abundance and might be overestimated by a factor of ~ 2. This ratio can also show spatial variations inside the cloud.

We derived an average H_2 density, $n(H_2)$, in the cloud core by dividing the peak value of the H_2 column density by the geometrical mean, d, of the major and minor diameters. The total mass in the cloud core was calculated for an uniform sphere with diameter d and average density $n(H_2)$, taking into account the mass of helium of 0.4 times the total hydrogen mass.
The excitation temperature at the centre of the cloud, 7.1 K, is lower than the temperatures derived in other dark clouds in the Cepheus-Cassiopeia region (Sato et al. 1994, Kun et al. 1994). On the other hand, the ^{13}CO optical depth is higher than in most of them; only the C^{18}O core 'E' in LDN 1251 containing a compact molecular outflow source has a similar value of the

Table 5. Derived parameters of the ^{13}CO cloud core in Kh 15 from the Nagoya-4m and Onsala-20m observations (see Fig. 6 and Fig. 7). The optical depth and column densities are average values over the core. Size, mass and number density are based on the distance of 250 pc.

	T_{ex} K	$\tau(^{13}CO)$	Δv kms^{-1}	$N(^{13}CO)$ 10^{15} cm^{-2}	$N(H_2)$ 10^{21} cm^{-2}	Size pc	$n(H_2)$ 10^3 cm^{-3}	Mass $M_\odot$
Nagoya-4m cloud	6.4	0.4	0.5	0.8	0.96	1.6×1.2	0.3	34
Nagoya-4m core	7.1	1.2	0.8	2.3	2.76	0.84×0.56	1.3	16
Onsala-20m core	7.3	1.3	0.8	2.2	2.64	0.77	1.2	13
Onsala-C1 core	7.3	1.6	1.0	4.1	4.92	0.10×0.20	7.1	1.5
Onsala-C2 core	7.5	1.5	0.9	3.7	4.44	0.17	5.0	1.7
Onsala-C3 core	7.2	1.8	0.8	3.8	4.56	0.14	5.5	1.1

^{13}CO optical depth (Sato et al. 1994). It should be noticed, that the ^{12}CO spectra (Fig. 2) apparently show self-absorption, which may account for the low excitation temperature. On the other hand, the excitation temperatures derived from the Onsala-20m ^{13}CO and C^{18}O spectra present very similar values (see next paragraph).

We have defined the cloud core in the map where $N(^{13}CO) \geq 1.2 \times 10^{15}\,cm^{-2}$, which has a size of $12' \times 8'$. The total gas mass in the cloud core is $16\,M_\odot$ (taking into account the helium mass), which is listed in the last column of Table 5. The total mass of the cloud inside the region with $N(^{13}CO) > 0.4 \times 10^{15}\,cm^{-2}$ ($\sim 6\sigma$ detection limit) was estimated to be $34\,M_\odot$. Thus, the ^{13}CO core contains at most 47% of the total mass of the cloud.

Onsala-20m: We mapped the central region of Kh 15, which remained unresolved by the Nagoya-4m beam. The ^{13}CO intergated intensity map (Fig. 7) shows three main condensations (cores), which we call C1, C2 and C3. The three cores shows the same geometrical structure as the corresponding I_{cold} cores (see also Fig. 7), although they appear at slightly different sky positions. Spatial differences may be due to the large ($\sim 5'$) size of the IRAS 100 μm detector pixels, and the upcoming HIRES processing. Therefore, we identify the CO-cores as the counterparts of the I_{cold} cores called the same. Because of the discrepancy of the CO and FIR map, we do not compare the distribution of molecular gas and dust in this finer scale. The derived properties of the Onsala C1, C2, C3 cores and the whole mapped region is summarized in Table 5. We calculated the ^{13}CO optical depth τ^{13} and the ^{13}CO column density $N(^{13}CO)$ as described in the previous subsection. The C^{18}O optical depth τ^{18} and column density $N(C^{18}O)$ were calculated following Nozawa et al. (1991). The derivation of the molecular hydrogen number density was done as described in the previous subsection, but in the positions where ^{13}CO was too thick optically ($\tau^{13} \geq 1.5$) we used the C^{18}O data to derived the molecular hydrogen number density as $N(H_2)\,/\,N(C^{18}O) = 9.2 \times 10^6$. This value was also derived as an average of the values listed in Harjunpää & Mattila (1996), as in the previous paragraph. The derivation of the number density of Onsala cores was done by removing the background molecular hydrogen column density value ($\sim 2.0 \times 10^{21}\,cm^{-2}$), and dividing the remaining by the effective diameter, d, of the core. Masses have been calculated using the sum of the background removed values of the ^{13}CO column density over the core. The central line velocities at the column density peaks of all the three cores are $3.2 \pm 0.1\,kms^{-1}$, and the noticed velocity shift in the Nagoya ^{13}CO data might be due the (relatively) coarse velocity resolution of those spectra, including the errors of the fits of the Gaussians.

5. Discussion

5.1. Comparison of various bands

We calculated the ratio between the dust mass and the mass of the gas in the Kh 15 core (see Sects. 4.2 and 4.3) and obtained $\sim$1:50 and $\sim$1:120 using the 15 K and the 17 K dust temperatures, respectively. Derivation of the mass of the gas using ^{13}CO relative abundances valid for star forming regions (e.g. Dickman 1978a and Duvert et al. 1986) yields an unrealistic gas-to-cold dust mass ratio of 20:1 or 50:1 when a dust temperature of 15 K or 17 K is assumed. It is unlikely that the cold dust temperature in Kh 15 is as high as $\sim$19 K which would be needed for a gas-to-dust mass ratio of 100:1. A dust temperature of 17 K, applied to calculate the dust mass, is an upper limit for the cold dust component in the Galaxy (see Lagache et al. 1998) and lower dust temperature values increase the dust mass.

Several papers investigated the relationship between the FIR intensities, the column density of CO isotopic lines and the visual extinction (see e.g. Laureijs et al. 1989, 1991, 1995). The ratio of the 100 μm intensity and the visual extinction varies from cloud to cloud between 2 and 10 $MJysr^{-1}mag^{-1}$ and usually a denser cloud shows a lower value of this ratio. The ratio of the 100 μm excess and the ^{13}CO (J=1–0) integrated intensity is in the range of 1.4 – 5.3 $MJysr^{-1}(Kkms^{-1})^{-1}$. We discuss these relationships for Kh 15 below.

To probe a larger area around Kh 15, we have constructed a scatter plot of the 100 μm emission I_{100}, derived from a galactic background removed ISSA plate for different subfields (see Table 1), and visual extinction A_V, derived from Wolf diagrams with the help of the method described in Sect. 4.1 (see Table 4). Removal of the $100\mu m$ galactic background emission was done following Boulanger & Pérault (1988). The slope of the linear least square fit is $6.6(\pm 2.8)\,MJysr^{-1}mag^{-1}$. Using $A_B = 1.3A_V$ (Dickman 1978b), the resulting slope for blue extinction 5.1 $MJysr^{-1}mag^{-1}$ is closed to 5.9 $MJysr^{-1}mag^{-1}$ obtained for LDN 1780 (Laureijs et al. 1995).

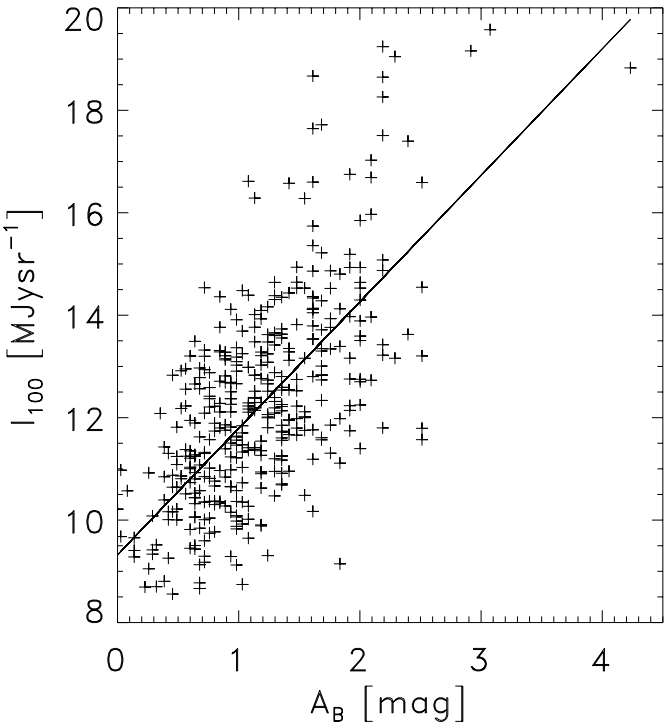

Fig. 8. Correlation between I_{100} and A_B. See the text below for the derived regression parameters.

Table 6. Results of the FIR emission – ^{13}CO (J=1-0) integrated intensity correlation analysis. The columns are: (1) the name of correlated quantities; (2) the slope of the linear fit; (3) the constant of the linear fit; (4) level of correlation

Correlated quantities	slope MJysr^{-1}[Kkms^{-1}]$^{-1}$	const. MJysr^{-1}	corr.
$I_{100}/W(^{13}CO)$	3.62±0.54	17.02±0.58	0.71
$\Delta I_{100}/W(^{13}CO)$	2.11±0.25	4.48±0.27	0.80

We have also investigated these correlations using our DSS star counts (See Sect. 3.1.2). Comparing the COBE calibrated HIRES 100 μm intensities averaged over the $3'\times3'$ sized reseau of the star count data, we have found the following relation for Kh 15:

$$I_{100} = (2.5\pm0.9)A_B\,\mathrm{MJysr^{-1}mag^{-1}} + (9.3\pm0.6)\,\mathrm{MJysr^{-1}}$$

(see also Fig. 8). The correlation coefficient is 0.72. The value of the slope is in a good agreement with the values found by Laureijs et al. (1995) towards the L134 cloud complex (2.1, 2.9 and 3.7 $\mathrm{MJysr^{-1}mag^{-1}}$ for LDN 183, LDN 134 and LDN 169, respectively; see their Table 2). The two distinct values of the slopes (5.1 $\mathrm{MJysr^{-1}mag^{-1}}$ and 2.5 $\mathrm{MJysr^{-1}mag^{-1}}$ from Wolf-diagrams and DSS star counts, respectively) are not in contradiction if we note that they probe regions of different densities and probably different dust compositions. In the outer regions of Kh 15 the 60 μm and 100 μm radiation is well correlated (indicating cirrus-like emission) and accordingly ΔI_{100} shows little variations, therefore the ΔI_{100} - A_B comparison is not presented here.

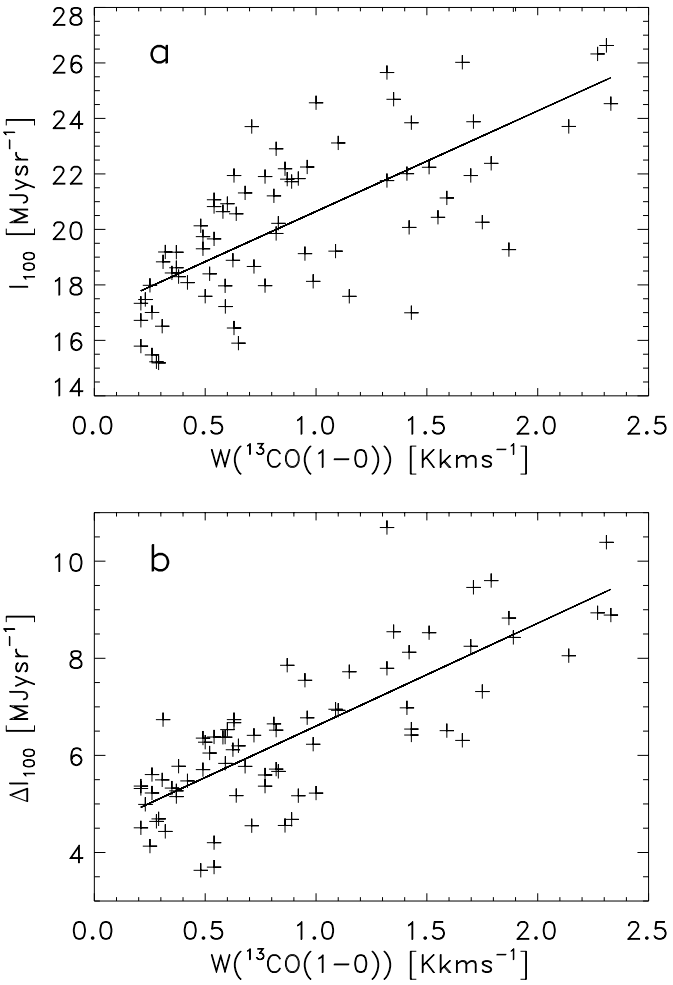

Fig. 9. Correlation between W(^{13}CO (J=1–0)) (Nagoya-4m) and I_{100} (**a**) and ΔI_{100} (**b**).

Assuming that integrated intensities of CO isotopic lines are proportional to I_{100} or ΔI_{100}, we have derived regression parameters from least-squares fits, presented in Fig. 9 and Table 6. To compare the Nagoya ^{13}CO (J=1–0) data and the 60 and 100 μm HIRES images, the latter have been convolved to Nagoya-4m resolution (2.′7). As one can see from Table 6 and Fig. 9a and b, W(^{13}CO $(1-0)$) is well correlated with both I_{100} or ΔI_{100}. The resulting parameters are close to the values found in other dark clouds e.g. by Laureijs et al. (1995).

5.2. Stability of Kh 15:

The dynamical state of the Kh 15 core was investigated following Liljeström (1991). If the gas motions in the ^{13}CO core are determined by gravitation only the relation between the three-dimensional velocity dispersion of the mean gas particle $\sigma_{\rm vir}$, the mass of the ^{13}CO core M and the effective radius of the ^{13}CO core $R_{\rm eff}$ is: $\sigma^2_{\rm vir} = C^2 \times M \times R^{-1}_{\rm eff}$, where the constant C depends on the cloud geometry and density structure. The derived three dimensional virialized velocity dispersion of the mean gas particle in the ^{13}CO core area is $\sigma_{\rm vir} = 0.37\,\mathrm{kms^{-1}}$ for

Table 7. Main parameters of Kh 15

distance	250 ± 25 pc
average visual extinction	$1\overset{\mathrm{m}}{.}6 \pm 0\overset{\mathrm{m}}{.}2$
peak visual extinction	$2\overset{\mathrm{m}}{.}4 \pm 0\overset{\mathrm{m}}{.}2$
size of the molecular cloud	1.6×1.2 pc
size of the molecular core	0.84×0.56 pc
total gas mass	$34\,M_\odot$
core gas mass	$16\,M_\odot$
peak hydrogen number density	5.9×10^3 cm^{-3}
FIR core cold dust mass	$\geq 0.12\ M_\odot$

a homogeneous sphere and $\sigma_{\rm vir} = 0.48\,{\rm kms}^{-1}$ for a centrally condensed ($\rho \propto {\rm R}^{-2}$) sphere. The typical observed ^{13}CO line width in the Kh 15 core is $\Delta {\rm v} = 0.80\,{\rm kms}^{-1}$. After correcting for the line broadening due to line opacity the ^{13}CO line width is $\Delta {\rm v} = 0.65\,{\rm kms}^{-1}$. Thus the three-dimensional velocity dispersion of the gas derived from observation is $\sigma_{\rm obs} = 0.55\,{\rm kms}^{-1}$ (see also Liljeström 1991). The ratio $\sigma_{\rm obs}/\sigma_{\rm vir}$ is 1.5 and 1.1 for a homogeneous and a centrally condensed sphere, respectively. These values are closed enough to 1 to justify that the cloud is probably in gravitational virial equilibrium, although the external pressure was neglected in this calculation.

The analysis can be repeated following Spitzer (1978, Eq. [11-24]), taking into account the external pressure as well. In this case we assumed spherical symmetry, uniform external pressure and no magnetic field or rotation. We defined a "dynamical" temperature of the ^{13}CO core as the Doppler temperature ${\rm T_D}$ corresponding to the line width of the ^{13}CO emission at the peak intensity (see e.g. Nozawa et al. 1991, Eq. [10]): ${\rm T_D} = \overline{\rm m}\Delta {\rm v}^2 (8{\rm ln2k})^{-1}$, where $\overline{\rm m}$ is the mean molecular mass, $\Delta {\rm v}$ is the full linewidth at half-maximum and k is the Boltzmann constant. This yielded ${\rm T_D} = 39\,{\rm K}$. The external pressure ${\rm P_{ext}}$ and its maximum value ${\rm P_{max}}$ have been estimated in the same manner as described by Nozawa et al. (1991, Sect. 4.2, Eq. [10-13]). We derived ${\rm P_{max}} = 1.9 \times 10^{-12}\,{\rm Nm}^{-2}$ and ${\rm P_{ext}} = 3.4 \times 10^{-13}\,{\rm Nm}^{-2}$ for Kh 15. We conclude that the cloud is in stable equilibrium, since $\log({\rm P_{max}}/{\rm P_{ext}}) = 0.74$ and ${\rm R} > {\rm R_{min}} = 0.16\,{\rm pc}$.

5.3. Connection of Kh 15 to its neighbourhood

We have shown in Sect. 4.1, that Kh 15 and the NW-part of GIRL126+10 are at similar distances ($250 \pm 25\,{\rm pc}$ and $200 \pm 20\,{\rm pc}$ respectively) within the uncertainities and taking into account the ~ 25 pc size of the loop. These distance of the loop is in an excellent agreement with the distance of LDN 1333.

Additional pointed ^{12}CO (J=1–0) line measurements around the loop show similar velocities at several positions (Tóth 1997, priv. com.). The CO velocities of the dark clouds Kh 19 (Khavtassi 1955) and LDN 1333 (see Fig. 10) are 3.2 kms^{-1} and 3.0 kms^{-1}, respectively. This implies that the distance of Kh 19 is similar to LDN 1333 i.e. ~ 200 pc. The existence of the loop GIRL126+10 is also confirmed by the principal component analysis (see e.g. Tóth et al. 1992) of HI velocity channel maps (from Hartmann & Burton 1997). This analysis shows the loop to be the most significant structure in the velocity interval $1\,{\rm kms}^{-1} \leq {\rm v_{LSR}(HI)} \leq 5\,{\rm kms}^{-1}$, and this 21 cm radiation is well correlated with the 100 μm FIR emission (Kiss et al. 2000, in prep.). Furthermore Kh 15 is elongated in the direction pointing into the center of the loop GIRL126+10, indicating an interaction between the cloud and the shell in the past.

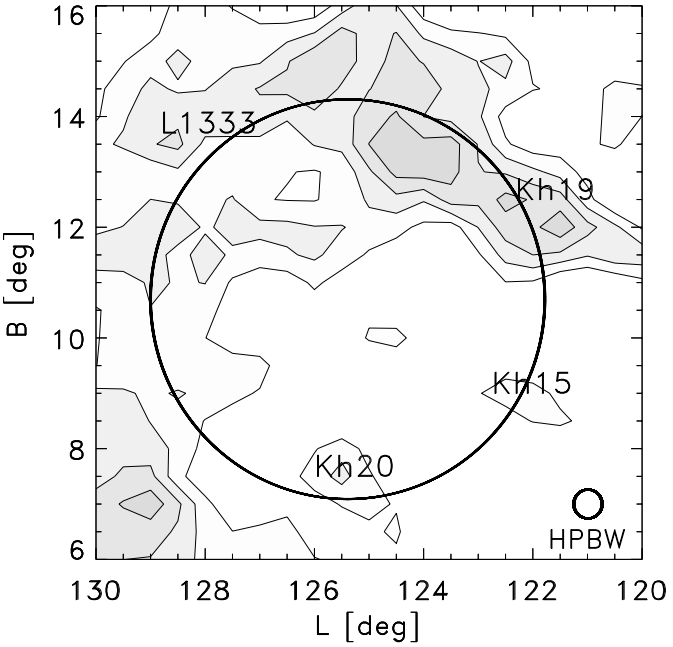

Fig. 10. HI 21 cm integrated intensity map of the FIR loop GIRL126+10 ($1\,{\rm kms}^{-1} \leq {\rm v_{LSR}} \leq 5\,{\rm kms}^{-1}$). Contours are from $130\,{\rm Kkms}^{-1}$ with $20\,{\rm Kkms}^{-1}$ steps.

We conclude from the collected multiwavelength data that Kh 15 is part of the loop structure seen at l=126°, b=10°, identified by us and called GIRL126+10.

5.4. The wall of the Local Bubble?

Table 4 shows the presence of a nearby extinction layer (at ${\rm d} \leq 150\,{\rm pc}$) appearing in most of the subfields of the Schmidt-plate. Sfeir et al. (1999) estimated the distance to the wall of the Local Bubble (LB) based on measurements of the equivalent widths of the NaI D line doublet, and distances measured by Hipparcos. They have found that the wall of the LB is located at $\sim$130 pc at this galactic longitude, at $|{\rm b}| \leq 10°$. This is in agreement with our estimation, thus we may consider this layer as the wall of the LB.

6. Summary

We presented the results of optical and radio observations and FIR data analysis of the Khavtassi 15 dark cloud. We determined its distance and average visual extinction from the optical measurements, gas mass and density from the radio, and dust properties from the FIR data. The main parameters of the cloud are summarized in Table 7 below.

We discussed the relationships between the ^{13}CO (1–0) integrated intensity, FIR emission and extinctions in the optical. We found similar relationships as in the case of the L134 cloud complex. Stability analysis shows that the cloud core is in stable equilibrium. We found the cloud to be most probably connected to a large FIR loop/shell seen around l=126°, b=10°. The wall of the Local Bubble probably lies at a distance of $\mathrm{d} \leq 150\,\mathrm{pc}$ in the direction of Kh 15.

Acknowledgements. We are indebted to L.G. Balázs and M. Kun for their valuable help and acknowledge the remarks of K. Mattila. S.N. appreciates very much the financial support of Petnica Science Center (Valjevo, Yugoslavia) for travel and stay at OSO during the observations, and the Onsala Space Observatory for the fellowship for the 1998/99 year.

This research has made use of data obtained through the High Energy Astrophysics Science Archive Research Center Online Service, provided by the NASA-Goddard Space Flight Center.

Onsala Space Observatory is the Swedish National Facility for Radio Astronomy and is operated by Chalmers University of Technology, Göteborg, Sweden, with financial support from the Swedish Natural Science Research Council and the Swedish Board for Technical Development.

The KOSMA radio telescope at Gornegrat–Süd Observatory is operated by the University of Köln, and supported by the Deutsches Forschungsgemeinschaft through grant SFB-301, as well as by special funding from the Land Nordrhein–Westfalen. The Observatory is administrated by the Internationale Stiftung Hochalpine Forschungstationen Jungfraujoch und Gornegrat, Bern, Switzerland.

This research was partially supported by the Hungarian Research Found (OTKA), under the number F-022566.

References

Boulanger F., Pérault M., 1988, ApJ 330, 964
Boulanger F., Bronfman L., Dame T.M., Thaddeus P., 1998, A&A 332, 273
Dame T.M., Ungerechts H., Cohen R.S., et al., 1987, ApJ 322, 706
Désert F.-X., Bazell D., Boulanger F., 1988, ApJ 334, 815
Désert F.-X., Boulanger F., Puget J.L., 1990, A&A 237, 215
Dickman R.L., 1978a, ApJS 37, 407
Dickman R.L., 1978b, AJ 83, 363
Duvert G., Cernicharo J., Baudry A., 1986, A&A 164, 349
Ebert R., 1994, ADASS III. ASP Conf. Ser. Vol. 61, p. 30
Grenier I.A., Lebrun F., Arnaud M., et al., 1989, ApJ 347, 231
Harjunpää P., Mattila K., 1996, A&A 305, 920
Hartmann D., Burton W.B., 1997, The Leiden/Dwingelo Survey of HI in the Galaxy. Cambridge University Press
Hauser M.G., Arendt R.G., Kelsall T., et al., 1998, ApJ 508, 25
Heathcote S.R., Brand P.W.J.L., 1983, MNRAS 203, 67
Hildebrand R.H., 1983, QJRAS 24, 267
Hubble E.P., 1934, ApJ 79, 8
Khavtassi J.Sh., 1955, Bulletin of Abastumani Astrophysical Observatory 18, 29
Khavtassi J.Sh., 1960, Atlas of Galactic Dark Clouds. Tbilisi
Kramer C., Degiacomi C.G., Graf U.U., et al., 1998, In: Philips T.G. (ed.) Proc. SPIE 3357, Advanced Technology MMW, Radio, and Terahertz Telescopes. p. 711
Kun M., Prusti T., 1993, A&A 272, 235
Kun M., Obayashi A., Sato F., et al., 1994, A&A 292, 249
Lagache G., Abergel A., Boulanger F., Puget J.-L., 1998, A&A 333, 709
Lang K.R., 1992, Astrophysical Data: Planets and Stars. Springer-Verlag
Laureijs R.J., Chlewicki G., Clark F.O., Wesselius P.R., 1989, A&A 220, 226
Laureijs R.J., Clark F.O., Prusti T., 1991, ApJ 372, 185
Laureijs R.J., Fukui Y., Helou G., et al., 1995, ApJS 101, 87
Lebrun F., 1986, ApJ 306, 16
Liljeström T., 1991, A&A 244, 483
Lynds B.T., 1962, ApJS 7, 1
Nozawa S., Mizuno A., Teshima Y., et al., 1991, ApJS 77, 647
Obayashi A., Kun M., Sato F., et al., 1998, AJ 115, 274
Ogawa H.S., McMullin D., Judge D.L., Canfield L.R., 1990, Journal of Geophysical Research Vol. 95, p. 4291
Sato F., Mizuno A., Nagahama T., et al., 1994, ApJ 435, 279
Seitter W.C., 1975, Bonner Spectral Atlas II, Ferdinand Dümmler Verlag
Sfeir D.M., Lallement R., Crifo, F., Welsh B.Y., 1999, A&A 346, 785
Spitzer L. Jr., 1978, Physical Processes in the Interstellar Medium. Wiley Interscience, New York
Taylor D.K., Dickman R.L., Scoville N.Z., 1987, ApJ 315, 104
Tóth L.V., Horváth A. Jr., 1996, In: Millar T.J., Raga A.C. (eds.) Shocks in Astrophysics. Kluwer
Tóth L.V., Walmsley C.M., 1996, A&A 311, 981
Tóth L.V., Balázs L.G., Ábrahám P., 1992, ADASS Conf. Ser. Vol. 25, p. 251
Tóth L.V., Haikala L.K., Liljeström T., Mattila K., 1995, A&A 295, 755
Tóth L.V., Kiss Cs., Moór A., 1996, In: Käufl H.U., Siebenmorgen R. (eds.) The Role of Dust in the Formations of Stars. ESO workshop, Springer, p. 125
Wainscoat R.J., Cohen M., Volk K., et al., 1992, ApJS 83, 111
Walker H.J., Cohen M., 1989, AJ 98, 2163
Wheelock S.L., Gautier T.N., Chillemi J., et al., 1994, IRAS Sky Survey Atlas Explanatory Supplement. JPL Publication, JPL, Pasadena, p. 94
Winnewisser G., Zimmermann P., Hernichel J., et al., 1990, A&A 230, 248
Wolf M., 1923, Astron. Nachr. 219, 109
Yonekura Y., Dobashi K., Mizuno A., et al., 1997, ApJS 110, 21